Role of screening and angular distributions in resonant x-ray emission of CO

Per Skytt,[1] Peter Glans,[2] Kerstin Gunnelin,[1] Jinghua Guo,[1] Joseph Nordgren,[1] Yi Luo,[3] and Hans Ågren[3]
[1]*Department of Physics, Uppsala University, Box 530, S-75121 Uppsala, Sweden*
[2]*Chemistry Department, University of Nevada Las Vegas, Box 454003, Las Vegas, Nevada 89154-4003*
[3]*Institute of Physics and Measurement Technology, Linköping University, S-58183, Linköping, Sweden*
(Received 18 March 1996)

Resonantly excited carbon and oxygen x-ray-emission spectra of gaseous carbon monoxide are presented. Emission spectra obtained with selective excitation to the π^* valence orbital and to various Rydberg levels are compared to satellite-free nonresonant spectra. Screening effects caused by the excited electron, creating energy shifts and intensity variations in the resonant spectra compared to the nonresonant spectra, are observed, as well as an angular dependence of the resonantly excited spectra. The experimental spectra are compared to simulated spectra where the vibronic part is computed by means of a lifetime-vibrational interference formalism. The electronic intensities are analyzed by a separate-state, self-consistent-field method and a formalism for resonant inelastic x-ray scattering, focusing on screening and angular dependence.
[S1050-2947(96)00812-8]

PACS number(s): 33.20.Rm, 33.50.Dq, 33.70.−w

I. INTRODUCTION

The rapid development of synchrotron radiation instrumentation in the past few years has spurred an increasing number of resonant x-ray-emission (RXE) studies in the soft-x-ray region [1]. The introduction of third-generation machines together with high-quality monochromators and matching end-station instrumentation has made several of these studies possible. The experimental achievements have to go hand in hand with theoretical formulations. A way to improve the basic understanding of the processes is to study simple systems where particular features of the processes can be distinguished in the spectra and compared with reliable calculations. Small molecules such as N_2,O_2, or CO are excellent test systems because of the possibility to model the electronic structure and the x-ray-emission process in detail by first-principles theory. Also, the diatomic molecules possess only one vibrational degree of freedom, which simplifies the analysis of the vibrational fine structure compared to larger systems with many vibrational modes. With only one, totally symmetric, vibrational mode one has, furthermore, the important simplification that polarization-, angular-, and symmetry-dependent features can be analyzed solely in terms of electronic-structure factors. In these systems the vibrational spacing and the lifetime broadening are of the same order of magnitude, leading to particular fine-structure effects [2–4], denoted lifetime-vibrational interference, which also have to be considered when describing the vibronic band profiles.

The majority of experimental studies have focused on solid-state samples where intensity considerations are less important than for diluted samples such as surface adsorbates [5] or gases. For experimental reasons it has only recently become possible to perform RXE studies in the ultrasoft-x-ray region on gas-phase systems [6]. Many interesting molecules, for example, those containing carbon, nitrogen, and oxygen atoms, emit x rays in this energy region. Molecular systems containing chlorine and sulphur atoms, emitting radiation at a few keV, have previously been studied with RXE [7,8]. These works as well as studies of optical fluorescence from molecules following valence ionization by synchrotron radiation [9] have shown that the angular and polarization distributions in some cases are anisotropic.

Despite the lack of experimental data, theoretical predictions of RXE spectra have appeared in the literature [10,11]. New theoretical formulations for describing resonant x-ray emission using a scattering approach [12,13] have highlighted the excitation-energy dependence of the emission spectra and also other properties, such as polarization anisotropy [14], interference effects [15], and symmetry selectivity [6,12,16,17], with no counterpart in nonresonant x-ray emission. Many of these features have been observed experimentally, but stringent tests of the models have been difficult due to the complexity of the studied samples.

In this work, experimental and theoretical efforts are combined on one small molecule, namely, CO, to highlight two particular properties of resonant x-ray emission. The *screening* of the core hole by the excited electron causes energy shifts and intensity variations in the resonant spectra compared to the nonresonant case. The linear polarization of the synchrotron radiation and the dipole nature of the absorption process create a preferential alignment of the randomly oriented molecules in the case of resonant excitation, producing an anisotropy in the *angular distribution* of the emitted x rays. The choice falls on CO also because this molecule has served as a showcase for nonresonant x-ray emission, with C K and O K spectra mapping the valence electronic structure differently according to the local selection rules. In this work, this characteristic feature is studied for the resonant case.

Nonresonant spectra recorded at conditions selected to suppress satellites are presented, and these are compared with resonant spectra excited to both the molecular π^* orbital and different Rydberg levels. The energy and intensity variations in the spectra are discussed and compared with theoretical predictions. Spectra recorded in different emission directions with respect to the polarization of the syn-

chrotron radiation are also presented and analyzed using theory of resonant inelastic x-ray scattering.

II. EXPERIMENT

A brief description of the experimental setup is given here, while a more detailed presentation is planned to be given elsewhere [18]. The experiments were made at beam line 7.0 [19] of the Advanced Light Source in Berkeley, California. This undulator beam line includes a spherical grating monochromator and is constructed to provide linearly polarized synchrotron radiation (SR) of high resolution and high flux with post-focusing mirrors capable of focusing the radiation to a narrow beam at the interaction region. This is crucial in these measurements because the grazing-incidence spectrometer [20] used to record the x-ray emission has a very small acceptance angle.

The spectrometer provides a choice of three different spherical gratings. It has an entrance slit with adjustable width and uses a two-dimensional multichannel detector that can be translated to the focal position defined by the Rowland circle of the grating in use. In these experiments a slit width of 20 μm was selected and gratings with 5 m radii and rule densities of 400 and 1200 lines/mm were used to record the carbon and oxygen K emission, respectively. The estimated resolution at full width at half maximum (FWHM) was about 0.8 and 0.7 eV, respectively.

The CO molecules were contained in a gas cell with thin windows transmitting most of the radiation. The SR entered the cell through a 1000-Å -thick silicon nitride window and the interaction region was viewed by the spectrometer through a 900-Å -thick polyimide window, supported by a polyimide grid and coated with 150 Å of aluminum nitride [21]. The spectrometer was mounted close to the interaction region with its entrance slit nearly parallel to the SR beam, thereby enabling a large fraction of the interaction region to be observed by the spectrometer. The gas pressure was optimized so that most of the SR was absorbed in the view of the spectrometer. In the spectra presented here the pressure ranged from a few tenths of a Torr to several Torr.

The vacuum chamber housing the spectrometer and gas cell arrangement can be rotated under vacuum around the axis defined by the SR beam [22] so that angle-resolved measurements can be carried out.

X-ray-absorption spectra were measured using the photocurrent from an electrode situated inside the gas cell. The signal was normalized with the photocurrent from a clean gold mesh introduced into the beam prior to the gas cell. These spectra were used to calibrate the excitation energy and to estimate the bandpass of the exciting radiation.

III. CALCULATIONS

Calculations of transition energies ($E_{ij}^{R,\mathrm{NR}}$) and intensities ($W_{ij}^{R,\mathrm{NR}}$) in both the resonant (R) and nonresonant (NR) cases are performed. $E_{ij}^{R,\mathrm{NR}}$ values are calculated as the energy difference of the two states (levels i,j) involved in the corresponding x-ray transitions and $W_{ij}^{R,\mathrm{NR}}$ values as the Einstein coefficients for spontaneous emission between initial and final states

$$W_{ij}=\frac{4\alpha E_{ij}^{3}}{3c^{2}}T_{ij}^{2}. \tag{1}$$

T_{ij} denotes the transition moments, c the speed of light, and α the fine-structure constant. We define and compute, furthermore, screening energies E_{ij}^{scr} and intensities W_{ij}^{scr} as

$$E_{ij}^{\mathrm{scr}}=E_{ij}^{R}-E_{ij}^{\mathrm{NR}} \tag{2}$$

and

$$W_{ij}^{\mathrm{scr}}=W_{ij}^{R}-W_{ij}^{\mathrm{NR}}, \tag{3}$$

where we assume that common energy levels $\{i,j\}$ of the two initial and the two final states in Eqs. (2) and (3) can be identified, i.e., that a quasiparticle (quasi-molecular-orbital) picture holds, so that it is meaningful to identify the shift in the spectra as due to screening of particular energy levels.

We have employed a numerical method that we originally developed for efficient computations of transition dipole matrix elements in nonresonant x-ray-emission spectra [23]. The method is described in the MOTECC-9X compilation of computational chemistry programs [24]. It handles the nonorthogonality problem in the evaluation of transition moments by utilizing efficient biorthogonalization [25] and configurational expansion schemes. Variational optimum of the core-hole states is obtained by employing a restricted configurational space for the core orbital and by applying the double, freeze-relaxation procedure described in Ref. [26]. We employ standard correlation consistent atomic natural orbital-type basis sets [27]: i.e., a $5s,4p,3d$ set and a standard correlating active space with one correlating orbital for each occupied valence orbital. This parametrization fulfills criteria for calculations of core-electron spectra, as given, e.g., in Refs. [24,28], and has been further tested in Ref. [29] in connection with calculations of x-ray spectra.

Unconstrained self-consistent-field (SCF) and multiconfigurational SCF (MCSCF) optimizations of each state involved in the resonant and nonresonant x-ray processes have been performed. In the resonant case that is the ground, core-excited, and valence-excited states and in the nonresonant case the ground, core-ionized, and valence-ionized states. The transition energies and intensities are then obtained in the vertical approach at the ground-state nuclear geometry as ΔSCF and ΔMCSCF values and the screening according to Eqs. (2) and (3) by subtracting two ΔSCF or two ΔMCSCF results.

IV. RESULTS AND DISCUSSION

In Secs. IV A and IV B experimental nonresonant spectra as well as π^{*} and Rydberg resonantly excited spectra are presented and their general character discussed. The spectra are compared to each other and emphasis will be put on energy shifts and intensity variations caused by the excited electron. Self-consistent-field calculations will then be used in Sec. IV C to discuss in more detail the origin of these energy shifts and intensity variations. In Sec. IV D spectra recorded at different angles with respect to the linear polarization of the exciting beam are presented. The angular dependence is discussed using a simple qualitative picture and compared with quantitative theoretical predictions.

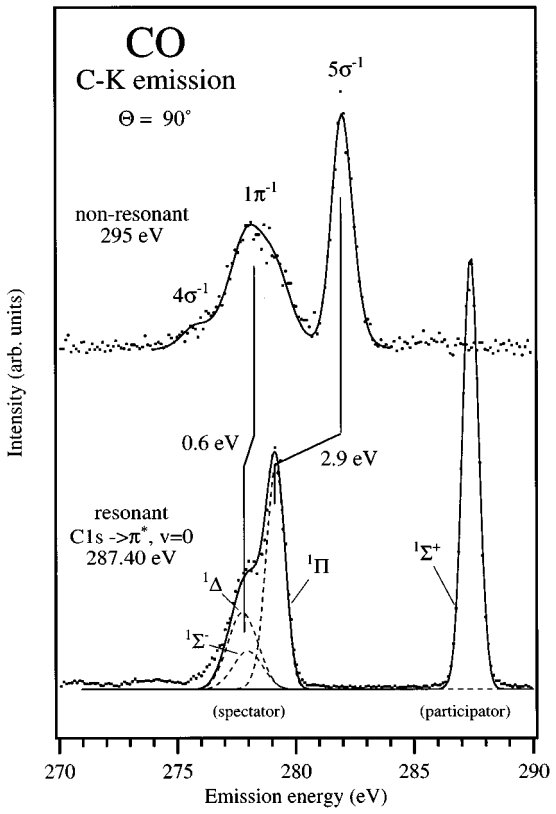

FIG. 1. Nonresonant (top) and resonant (bottom) carbon x-ray-emission spectra of CO. A *satellite-free* nonresonant spectrum was obtained by tuning the excitation energy just a few eV above the C $1s$ ionization threshold (below the shake-up and shake-off thresholds). An excitation energy of 287.4 eV (corresponding to the $v=0$ vibrational level of the C $1s^{-1}\pi^*$ state) was used to record the RXE spectrum. The energy shifts for the 1π and 5σ emission bands caused by the π^* spectator electron are indicated. The solid lines are simulated vibrational band profiles (see text for details).

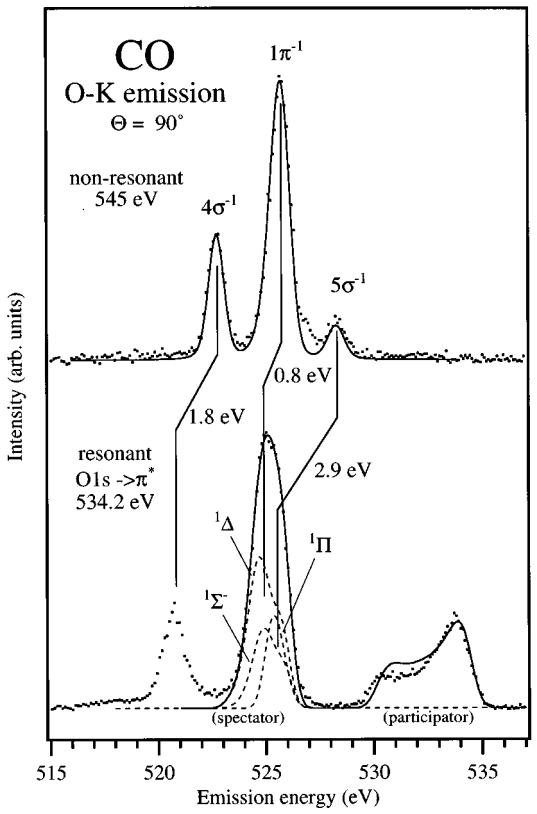

FIG. 2. Satellite-free, nonresonant (top) oxygen x-ray-emission spectrum of CO and an oxygen π^* RXE spectrum (bottom). The resonant spectrum was excited to the maximum of the π^* absorption band (at 534.2 eV). Energy shifts for the $5\sigma, 1\pi$, and 4σ emission bands caused by the π^* electron are indicated. The solid lines show the simulated vibrational band profiles.

A. Nonresonant spectra

The ground-state configuration of CO can be written as $(1\sigma)^2(2\sigma)^2(3\sigma)^2(4\sigma)^2(1\pi)^4(5\sigma)^2\,{}^1\Sigma^+$, where 1σ and 2σ correspond to the two $1s$ core orbitals localized on the oxygen and carbon sites, respectively. 3σ represents the inner valence orbital and the remaining three molecular orbitals are outer valence orbitals. Nonresonant x-ray emission is obtained when a core-ionized state decays to a valence ionized state by a valence electron filling a vacancy in the 1σ or 2σ orbital. Experimental nonresonant carbon and oxygen x-ray-emission spectra are presented in Figs. 1 and 2 (top spectra). The dipole nature of the emission process together with the localized character of the core-hole states will make the spectral intensities of each band dependent on the local (core-hole centered) $2p$ population, i.e., the one-center contribution [30]. The outermost valence orbital in CO, the 5σ orbital, has most of its $2p$ weight on the carbon site, which results in high intensity in the carbon x-ray-emission spectrum at 282.0 eV. The low weight of this orbital on the oxygen site leads to a low spectral intensity in the oxygen spectrum at 528.3 eV. The 1π orbital, on the other hand, is distributed on both atoms, as can be concluded by the high intensity in both the carbon and oxygen spectrum at 278.4 and 525.5 eV, respectively. The 4σ has predominantly oxygen character and very little carbon $2p$ character. The remaining valence orbital 3σ is effectively one-center forbidden and, furthermore, subject to strong correlation breakdown (a prediction of four major breakdown states is given in Ref. [31]) and is practically unobservable in nonresonant spectra [32].

The spectra presented were recorded with the excitation energy set just a few eV above the corresponding ionization thresholds to minimize the influence of *initial-state* shake-up or shake-off satellites obscuring the interpretation of the spectra [33]. Nonresonant, electron-beam excited x-ray spectra of CO recorded with higher instrumental resolution have been presented previously [34,35]. In these spectra even vibrational fine structure was resolved, but due to the high-energy excitation those spectra also exhibit satellites that overlap with the pure bands making relative intensities difficult to obtain. The photographic plate detection, which was used in those measurements, also makes the measured intensities uncertain. Therefore, the nonresonant, satellite-free spectra presented in this paper provide more reliable relative intensities and band shapes. In addition, the nonresonant spectra were recorded at the same experimental conditions (resolution and dispersion) as the resonant ones, which enables an accurate determination of relative energies between the resonant and nonresonant spectra. This is, as will be

shown later on, of importance in the current investigation. The emission energy scales were adjusted in such a way that the energy positions of simulated vibrational band profiles, obtained using known literature values, were in good agreement with those in the π^* RXE spectra presented in Figs. 1 and 2 (bottom spectra). These energy scales were then used in all the resonant and nonresonant spectra.

The widths of the different bands are, apart from the instrumental broadenings, given by vibrational fine structure. Core ionization leads, in general, to bond length changes, causing excitation of several vibrational levels [36]. This is the case for carbon monoxide C $1s$ ionization (significant bond shortening). The nuclear conformation of the core-ionized state may, however, remain close to that of the ground state, with little vibrational excitation as a result. This is the situation for O $1s$ ionization (slight bond lengthening). Explanations to these different behaviors have been given in Refs. [37,38]. Subsequent decays involving a nonbonding orbital, such as the 5σ orbital, result in small bond length changes and the width of the x-ray-emission band becomes determined mostly by the core excitation. Involvement of a bonding orbital, such as the 1π, on the other hand, will cause a large bond lengthening and hence a broad vibrational progression, as can be exemplified by the $1\pi^{-1}\ ^1\Pi$ band in the carbon spectrum. One can also note that even if the final states of the x-ray-emission process are the same as for valence photoemission, the vibrational envelopes are different because of the involvement of the intermediate core-ionized state in the x-ray process. The spectral profiles can be simulated using known potential-energy curves for the different states involved: the ground, the core-ionized intermediate, and the valence-ionized final states. Franck-Condon calculations using Morse potentials have been carried out. The result is used together with lifetime-vibrational interference (LVI) theory for simulations of the emission bands [12,39]. The simulated profiles are drawn with solid lines in the figures. The potential-energy curve parameters are given in Table I. The lifetime widths at FWHM used in the simulations are 0.097 eV for the C $1s^{-1}\ ^2\Sigma^+$ state [42] and 0.18 eV for the O $1s^{-1}\ ^2\Sigma^+$ state [44]. To account for the spectrometer's instrumental resolution the final profiles were convoluted with Gaussian functions, with full widths at half maxima of 0.8 and 0.7 eV, respectively. The relative intensities of the different bands in the nonresonant spectra are given in Table II, together with band energies measured at the center of gravity of each band. The 4σ band in the oxygen spectrum has been included for completeness, but will not be treated any further. Also included in Table II are experimental and calculated energies and intensities for the π^* RXE spectra.

TABLE I. Spectroscopic constants of the Morse potential-energy curves used in the simulation of the vibrational band profiles. ω_e is the vibrational energy, $\omega_e x_e$ the anharmonicity constant, R_e the equilibrium internuclear distance, and E_{00} the excitation energy from the ground state to the lowest ($v=0$) vibrational level of the excited state.

State	$\omega_e(\mathrm{cm}^{-1})$	$\omega_e x_e(\mathrm{cm}^{-1})$	R_e (Å)	E_{00} (eV)
$X\ ^1\Sigma^+$ (g.s.)[a]	2169.813	13.2883	1.128323	0
C $1s^{-1}\ ^2\Sigma^+$[b]	2599	15.92	1.073	295.9
O $1s^{-1}\ ^2\Sigma^+$[c]	1931.7	10.93	1.153	542.1
$5\sigma^{-1}\ ^2\Sigma^+$[d]	2214.24	15.16	1.1151	14.014
$1\pi^{-1}\ ^2\Pi$[d]	1562.06	13.53	1.2437	16.544
$4\sigma^{-1}\ ^2\Sigma^+$[d]	1734.18	27.927	1.1687	19.772
C $1s^{-1}\pi^*\ ^1\Pi$[d]	2083.55	15.32	1.1529	287.41
O $1s^{-1}\pi^*\ ^1\Pi$[e]	1426.1	18.77	1.28	533.4[f]
$5\sigma^{-1}\pi^*\ A\ ^1\Pi$[a]	1518.2	19.40	1.2353	8.068
$1\pi^{-1}\pi^*\ I\ ^1\Sigma^-$[a]	1092.22	10.70	1.3911	8.069
$1\pi^{-1}\pi^*\ D\ ^1\Delta$[a]	1094	10.20	1.399	8.174

[a]Parameters are taken from Ref. [40].
[b]Parameters are taken from Ref. [41].
[c]Parameters are taken from Ref. [36].
[d]Parameters are taken from Ref. [42].
[e]Parameters are taken from Ref. [4].
[f]Parameters derived from the vertical energy in Ref. [43].

B. Resonant spectra

1. π^* resonance

Instead of core ionizing the molecule it is possible to populate an unfilled valence or Rydberg orbital selectively by choosing a suitable energy of the exciting radiation. In Figs. 1 and 2 (lower part) carbon and oxygen π^* RXE spectra are presented. The carbon spectrum was recorded with the excitation energy tuned to the $v=0$ vibrational level at 287.40 eV. The bandpass of the exciting photon beam was set to 0.20 eV at FWHM. Two salient features are observed in the spectrum: the high-energy one positioned at about 287 eV can be identified as a participator transition in which the excited electron fills the core hole, while the other broader double-peak feature in the 276–280 eV energy region is due to so-called spectator transitions in which the excited electron remains as a spectator while a valence electron fills the core hole. This spectrum differs from the nonresonant one (top spectrum) by the appearance of the strong participator peak and shifts of the spectator transitions to lower energies. These energy shifts can be interpreted as a result of a screening effect by the π^* electron and this will be thoroughly discussed in Sec. IV C. The participator peaks will not be further considered here, but we notice that the peak intensity and shape are affected by self-absorption and absorption by the exit window, making intensity determinations more difficult [39].

For the oxygen spectrum in the lower part of Fig. 2, the excitation energy was set to 534.2 eV, near the maximum of the broad π^* x-ray-absorption band [45]. The bandpass of the exciting photon beam was determined from a measured x-ray-absorption spectrum to be about 0.65 eV. Like in the carbon case, a participator band as well as energy shifts of the spectator transitions when compared to the corresponding transitions in the nonresonant spectrum (top part) can be observed. In this case the participator band is much broader and it has a long low-energy tail indicating that a large number of vibrational levels are excited in the final (ground) state. This is due to the large equilibrium bond length difference between the ground and core-excited state.

The final states of the spectator transitions are neutral valence-excited states, whereas in the nonresonant case they are singly charged valence-ionized states. For the CO mol-

TABLE II. Experimental π^* resonant (E_R) and nonresonant (E_{NR}) energies and relative intensities (I_R,I_{NR}) for the 5σ and 1π x-ray-emission bands of CO. (The intensities in the π^* RXE spectra are corrected for the angular dependence so that they are proportional to the I_0 values, defined in Sec. IV D.) The experimental values are compared with computed energies and intensities (in parentheses), which are normalized in the same way as the experimental data.

Emission band	E_R (eV)	I_R	E_{NR} (eV)	I_{NR}
		Carbon		
5σ	279.1 (279.3)	1.25 (1.10)	282 (282.9)	0.86 (0.88)
1π	277.8 (277.9)[a]	1 (1)[a]	278.4 (279.6)	1 (1)
		Oxygen		
5σ	525.4 (525.3)	0.24 (0.20)	528.3 (528.2)	0.13 (0.07)
1π	524.9 (523.9)[a]	1 (1)[a]	525.5 (525)	1 (1)
4σ	520.7		522.7	0.24

[a]The values for the $1\pi^{-1}\pi^{*}\,{}^1\Delta$ and ${}^1\Sigma^-$ bands are used.

ecule the final states of the spectator transitions are $5\sigma^{-1}\pi^{*}\,{}^1\Pi$ and $1\pi^{-1}\pi^{*}\,{}^1\Delta,{}^1\Sigma^-$, and ${}^1\Sigma^+$ along with $4\sigma^{-1}\pi^{*}\,{}^1\Pi$. The strongest spectator transitions are to the first three of these states. In the oxygen case transitions to the $4\sigma^{-1}\pi^{*}\,{}^1\Pi$ state also give rise to a fairly strong emission peak. Transitions to the ${}^1\Sigma^+$ state, on the other hand, are expected to be weak in both the carbon and oxygen RXE spectra according to our calculations and there is no obvious feature in the RXE spectra that can be assigned to this final state. The calculations also predict that this state has a 5.5 eV higher energy than the two almost degenerate ${}^1\Sigma^-$ and ${}^1\Delta$ states. This will be discussed in Sec. IV C.

Simulations of vibrational band profiles using LVI theory have been performed also for the RXE spectra. The band profiles for the participator peak and for the spectator transitions to the $5\sigma^{-1}\pi^{*}\,{}^1\Pi$ and $1\pi^{-1}\pi^{*}\,{}^1\Delta$ and ${}^1\Sigma^-$ final states were simulated using potential curves for the ground, core-excited, and valence-excited states. The potential-energy curve parameters are given in Table I. The lifetime widths at FWHM used in the simulations are 0.18 eV for the O $1s^{-1}\pi^{*}\,{}^1\Pi$ state [44] and 0.086 eV for the C $1s^{-1}\pi^{*}\,{}^1\Pi$ state [42]. The relative intensities for the spectator transitions were determined from the experimental spectra by fitting the simulated profiles. The obtained values are given in Table II. A thorough analysis and discussion of the band profiles in the π^* RXE spectra can be found in the following paper [39], in which π^* RXE spectra recorded at other excitation energies are also studied.

2. Rydberg resonances

Carbon RXE spectra were also recorded by exciting to the $3s\sigma$ and $3p\pi$ Rydberg resonances. These spectra are shown in Fig. 3. The bandpass of the exciting photon beam was set to about 0.4 eV for the $3s\sigma$ RXE spectra and about 0.25 eV for the $3p\pi$ RXE spectra. These x-ray-emission spectra appear more like the nonresonant spectra in terms of energy positions. The participator peaks in these spectra are very weak due to small transition moments and they were not observed. The spectra clearly show the excitation-energy dependence of the vibrational band profiles as well as an angular dependence of the relative intensities. The energy dependence can be ascribed to the vibrational selectivity in the excitations. The $3p\pi$ RXE spectra were recorded with the excitation energies tuned to $v=0$ and 1 vibrational levels, respectively. The emission peak at 278 eV, corresponding to $1\pi^{-1}3p\pi$ final states, changes from a single band in the $v=0$ spectra to a broader double-peak band in the $v=1$ spectra. In a simplified semiclassical Franck-Condon picture the decay transitions occur preferentially at the classical turn-

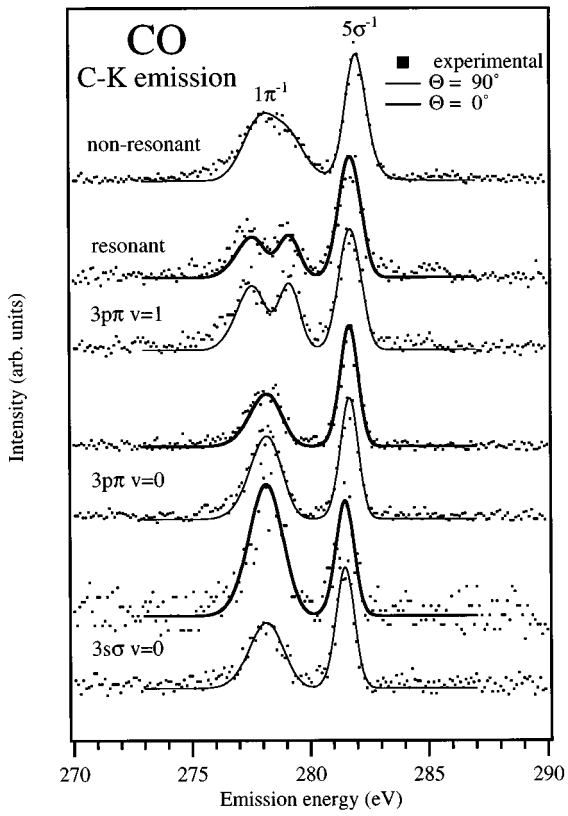

FIG. 3. Carbon RXE spectra excited to $3s\sigma$ ($v=0$) and $3p\pi$ ($v=0$ and $v=1$) Rydberg resonances. Spectra recorded at both $\theta=0°$ and 90° are presented. A nonresonant spectrum is included for comparison. All the spectra were normalized to have the same peak height for the 5σ band. The solid lines show the simulated vibrational band profiles.

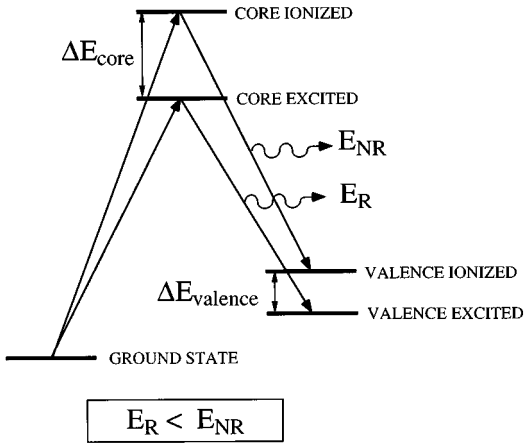

FIG. 4. Schematic energy-level diagram for the states involved in nonresonant and resonant x-ray emission.

ing points of the vibrations, except for the $v=0$ vibrational level where the decays occur primarily at the equilibrium bond distance. The final states for the emission band at 278 eV have an equilibrium bond length that is substantially longer than that of the intermediate core-excited state. The emission band is therefore broad. At the outer turning point of the $v=1$ vibrational level the nuclear distance is closer to the equilibrium distance of the final state and low vibrational levels of the final state are populated, while at the inner turning point, which is far from the equilibrium distance of the final state, much higher vibrational levels are populated. Therefore the emission energy is different for decay from the two turning points. This explains qualitatively the dramatic change of the emission band at 278 eV, from a single to a double-peak feature, although the excitation energy was changed only 0.3 eV. Vibrational band profile simulations, taking LVI effects into account, were performed also for these spectra. The same potential-energy curves as for the core- and valence-ionized states were then used, but shifting the spectra 0.1–0.5 eV to lower energies to account for the energy shift caused by the presence of the spectator electron. The simulated profiles reproduced the observed band-shape variations very well, as Fig. 3 shows. The fact that the band profiles are modeled satisfactorily with these potential-energy curves is a manifestation of the small screening induced by the Rydberg spectator electrons. The angular dependence of the relative band intensities will be discussed in detail in Sec. IV D.

C. Screening

The presence of a spectator electron affects the emission energies for the spectator transitions. In Sec. III we defined a screening energy, also called a spectator shift, as the difference between resonant and nonresonant x-ray-emission energies for decay transitions involving the same valence orbital. This energy shift is illustrated by a state diagram in Fig. 4. The screening energy is determined by the difference between ΔE_{core} and $\Delta E_{\text{valence}}$, where ΔE_{core} and $\Delta E_{\text{valence}}$ correspond to the ionization energies for the spectator electron in the presence of a core and valence hole, respectively [cf. Eq. (2)]. Because spectator electrons, in general, are more tightly bound in the presence of a core hole than in the presence of a valence hole, the screening energies will be negative, i.e., the spectator bands in RXE spectra appear at lower energies than the corresponding bands in the nonresonant spectra. The magnitudes of the screening energies depend on to which degree the spectator electron penetrates the molecular ion core. For a nonpenetrating, Rydberg-like orbital, the shifts are therefore expected to be small.

From our spectra in Figs. 1–3, experimental screening energies were determined from the energy positions measured at the centers of gravity of the different bands. The screening energies for the π^* RXE spectra are summarized in Table III. A statistical average of the energy positions of the emission bands to the near-degenerate $^1\Delta$ and $^1\Sigma^-$ final states were used to obtain the emission energy in the π^* RXE spectra for the 1π emission band. The magnitude of the screening energies induced by the π^* electron is larger for the 5σ emission bands than for the 1π emission bands: -2.9 versus -0.6 eV in the carbon case and -2.9 versus -0.8 eV in the oxygen case. From the carbon $3s\sigma$ $(3p\pi)$ Rydberg-excited RXE spectra the screening energies are derived to be about -0.5 (-0.3) eV for the 5σ band and -0.2 (-0.1) eV for the 1π band. The nonpenetrating character of the Rydberg orbitals is thus illustrated by the smaller magnitude of the screening energies in the case of Rydberg excitations.

It is also possible to derive the screening energies from intermediate- and final-state energies given in literature. Vertical binding energies from photoelectron spectra can be used for the core-ionized (C_{BE}) and valence-ionized (V_{BE}) states and vertical absorption energies for the core-excited (C_{AE}) and valence-excited (V_{AE}) states. The screening energy can be calculated from these values as

$$E^{\text{scr}}=(C_{\text{AE}}-V_{\text{AE}})-(C_{\text{BE}}-V_{\text{BE}}), \tag{4}$$

TABLE III. Screening energies (in eV) obtained from the x-ray-emission spectra are compared to experimental values, derived from *vertical* binding and absorption energies obtained as the center of gravity (CG) or from potential-energy curves, and to calculated energies. For the 1π emission band the E^R values were obtained assuming statistical intensity ratios for transitions to the $^1\Delta$ and $^1\Sigma^-$ final states. (C) and (O) refer to the site (carbon or oxygen) of the core hole.

Emission band	$E^R_{\text{expt}}-E^{\text{NR}}_{\text{expt}}$	$E^R_{\text{vert CG}}-E^{\text{NR}}_{\text{vert CG}}$ [a]	$E^R_{\text{vert}}-E^{\text{NR a}}_{\text{vert}}$	$E^R_{\text{calc}}-E^{\text{NR}}_{\text{calc}}$
5σ (C)	-2.9	-3.2	-3.2	-3.6
1π (C)	-0.6	-1.5	-1.7	-1.7
5σ (O)	-2.9	-2.3	-2.3	-2.9
1π (O)	-0.8	-0.6	-0.8	-1

[a] $E^R_{\text{vert}}=(C_{\text{AE}}-V_{\text{AE}})$ and $E^{\text{NR}}_{\text{vert}}=(C_{\text{BE}}-V_{\text{BE}})$ were used to determine $E^R_{\text{vert}}-E^{\text{NR}}_{\text{vert}}$; see Table IV.

TABLE IV. Experimental vertical energies measured as center of gravity $E_{\text{vert CG}}$ and from potential-energy curves E_{vert}; see Table I. The core (C_{BE}) and valence (V_{BE}) binding energies are obtained from photoelectron data, while the core (C_{AE}) and valence (V_{AE}) excitation energies are obtained from absorption data.

Energy	Final state	$E_{\text{vert CG}}$ (eV)	E_{vert} (eV)
C_{BE}	C $1s^{-1}\,^2\Sigma^{+}$ [a]	296.15	296.10
	O $1s^{-1}\,^2\Sigma^{+}$ [b]	542.10	542.15
V_{BE}	$5\sigma^{-1}\,^2\Sigma^{+}$ [c]	14.03	14.02
	$1\pi^{-1}\,^2\Pi$ [c]	17.10	17.12
	$4\sigma^{-1}\,^2\Sigma^{+}$ [c]	19.77	19.87
C_{AE}	C $1s^{-1}\pi^{*}\,^1\Pi$ [d]	287.43	287.45
	O $1s^{-1}\pi^{*}\,^1\Pi$ [e]	534.30	534.36
V_{AE}	$5\sigma^{-1}\pi^{*}\,^1\Pi$ [f]	8.49	8.56
	$1\pi^{-1}\pi^{*}\,^1\Delta$ [f]	9.93	10.21
	$1\pi^{-1}\pi^{*}\,^1\Sigma^{-}$ [f]	9.75	9.98

[a]Energies are taken from Ref. [41].
[b]Energies are taken from Ref. [36].
[c]Energies are taken from Ref. [46].
[d]Energies are taken from Ref. [42].
[e]Energies are taken from Ref. [4].
[f]Energies are taken from Ref. [40].

which agrees with the definition of the computed screening energies in Eq. (2). Screening energies obtained using the values in Table IV are listed in Table III. There are obvious deviations between these screening energies and those obtained from our spectra. The deviations are due to that the vibrational envelopes in x-ray emission are different from those of transitions involving the same final states in photoelectron and absorption spectra. The reason is that the nonnegligible lifetime of the intermediate, core-hole state results in that the internuclear distance may change before the x-ray-emission decay occurs.

The screening energies depend on the penetrating character of the spectator electron. However, the details of the screening mechanism are a bit more complex than that. We have performed calculations of the screening energies at different levels of approximation to gain more detailed information on what contributions are significant for the energy shifts in the π^* RXE spectra of CO. The calculations were carried out at the ground-state equilibrium geometry for all states, i.e., assuming the vertical approach. This means that the screening energies are evaluated from the intersection points of the potential-energy curves with a vertical line at the equilibrium bond distance of the ground state. The calculated screening energies can be decomposed into electrostatic, relaxation, and correlation contributions, as was described in more detail in Ref. [29]. The electrostatic value is calculated by subtracting total energies of the involved states using Hartree-Fock calculations with frozen ground-state orbitals. The relaxation contribution is obtained by subtracting the electrostatic contribution from the screening energies obtained by full SCF calculations using optimized wave functions and the correlation contribution is obtained by subtracting the SCF values from the full MCSCF values. We list decomposed screening energy contributions for the 5σ orbital in Table V. We observe consistent trends in both the oxygen and carbon cases. The presence of the π^* spectator electron gives negative electrostatic contributions to the screening energies of a little more than 1 eV. Relaxation gives the most important contribution to the screening energies in both cases: $\simeq -3$ eV for carbon and $\simeq -2$ eV for oxygen. Compared to these values, the lowering of the magnitude of the screening energies by the correlation is small, roughly 0.5 eV in both cases. Table V also lists the magnitude of the *penetration relaxation* defined as the difference between screening obtained by calculations using the full SCF and the SCF with the π^* level frozen. We note that this relaxation gives energies close to the SCF values, which includes electrostatic and relaxation contributions, indicating that it is the spectator π^* electron that causes the large relaxation contributions to the screening energies.

In Tables III and VI the MCSCF calculated screening energies for the 5σ and 1π emission bands are included. The MCSCF values in the carbon and oxygen cases are -3.6 and -2.9 eV for the 5σ orbital and -1.7 and -1.0 eV for the 1π orbital. Because these values were calculated using the *vertical* approach they are expected to be in better agreement with the values deduced from photoelectron and absorption data [Eq. (4)]. There are differences between center-of-gravity and vertical energies also for absorption spectra. However, as seen in Tables III and IV, these corrections are sufficiently small to be neglected in the present context.

Calculated MCSCF transition and screening intensities are presented in Table VI. The calculations show that the intense C $1s$ to 5σ transitions have almost the same strength in both the resonant and the nonresonant cases; the magnitude of the screening intensity is only about 4% of the total nonresonant intensity in this case. For the weak O $1s$ to 5σ transitions the screening intensity is much larger and in fact of the same order as the total nonresonant intensity. The magnitudes of the screening intensities for the 1π emission

TABLE V. Different contributions to the screening energies (in eV) and intensities of the 5σ x-ray-emission band. [Intensities are represented by squared transition moments (in a.u.) times $10^{-3}=1.929\times10^{6}W/E^{3}$, where W is the Einstein coefficient and E the transition energy.] The different entities are deduced from calculations performed at different levels of approximations ranging from frozen orbital to MCSCF calculations (see the text for more details).

Contribution	C energy	C intensity	O energy	O intensity
electrostatic	-1.228	0.653	-1.277	0.451
relaxation	-3.133	-1.036	-2.029	-0.305
correlation	0.815	0.243	0.415	0.384
penetration relaxation	-3.827	-0.419	-3.119	0.086

TABLE VI. Computed transition energies (E) in eV and intensities (I) for nonresonant (NR) and π^* resonant (R) 5σ and 1π x-ray-emission bands of CO. [Intensities are given by squared transition moments (in a.u.) times $10^{-3}=1.929\times10^{6}W/E^{3}$, where W is the Einstein coefficient and E the transition energy.]

Final state	E_R	I_R	E_{NR}	I_{NR}	E_{scr}	I_{scr}
			Carbon			
$5\sigma^{-1}\,^2\Sigma^+$			282.888	3.596	−3.55	−0.140
$5\sigma^{-1}\pi^*\,^1\Pi$	279.342	3.456				
$1\pi^{-1}\,^2\Pi$			279.625	4.088	−1.649[a]	−0.889[b] (0.103[c])
$1\pi^{-1}\pi^*\,^1\Delta$	277.976	2.094				
$1\pi^{-1}\pi^*\,^1\Sigma^-$	277.788	1.050				
$1\pi^{-1}\pi^*\,^1\Sigma^+$	272.265	0.055				
			Oxygen			
$5\sigma^{-1}\,^2\Sigma^+$			528.239	0.399	−2.891	0.530
$5\sigma^{-1}\pi^*\,^1\Pi$	525.348	0.929				
$1\pi^{-1}\,^2\Pi$			524.981	6.072	−0.978[a]	−1.153[b] (−0.128[c])
$1\pi^{-1}\pi^*\,^1\Delta$	524.002	2.973				
$1\pi^{-1}\pi^*\,^1\Sigma^-$	523.802	1.485				
$1\pi^{-1}\pi^*\,^1\Sigma^+$	518.277	0.461				

[a]With respect to the $1\pi^{-1}\pi^*\,^1\Delta$ state; see the text for details.
[b]Using the sum of the $^1\Delta$,$^1\Sigma^-$, and $^1\Sigma^+$ intensities.
[c]Assuming that the intensity of $^1\Sigma^+$ is half that of $^1\Delta$.

bands are calculated to be about 20% of the nonresonant intensities. However, if we adjust the transition intensity to the $1\pi^{-1}\pi^*\,^1\Sigma^+$ final state, which is depleted by configuration mixing, by assuming that this transition statistically has half the intensity of the transition to the $^1\Delta$ state, the screening intensities are only a few percent in both the carbon and the oxygen cases (see values in parentheses in Table VI).

The difference in screening intensities for the C 1s to 5σ and O 1s to 5σ transitions can probably be traced to the particular localization of the 5σ and π^* orbitals, both being mainly centered on the carbon site. Much of the screening of a core hole on the oxygen site takes place through the other valence electrons rather than through the π^* electron. Partly this is effectuated by the 5σ electrons, and the O character of this orbital increases. Since the O p-type character of 5σ is so small to start with, a small increase will have a large relative effect on the emission intensity. The C 1s to π^* excitation, on the other hand, leads directly to screening of the core by the π^* electron, without much further rearrangement of the other electrons (the π^* level is self-screening for C 1s excitation). The emission intensity from the C 1s to 5σ transition is therefore not expected to change so much compared to the nonresonant case. The relative screening intensity for 5σ emission is therefore larger in the oxygen case than in the carbon case.

In Table V one notes significant cancellation effects for the different contributions to the screening intensities for the C 1s to 5σ and O 1s to 5σ transitions. Relaxation gives a negative contribution, while the electrostatic and correlation contributions are positive. The penetration relaxation value for the screening intensity of the O 1s to 5σ transition is close to zero, which supports our previous statement that the O 1s core hole is not screened that much by the π^* electron, but rather by the other valence electrons.

The higher energy (5.5 eV higher) of the $1\pi^{-1}\pi^*\,^1\Sigma^+$ state is common for organic molecules and is associated with the valence character of the 1π and π^* orbitals and a large one-center two-electron repulsion interaction for this particular state. The splitting between the $^1\Sigma^-$ and $^1\Delta$ states of the $1\pi^{-1}\pi^*$ configuration is, on the other hand, determined by a much weaker (one-center) exchange interaction, and these states remain quasidegenerate even if π^* is a compact level [47]. We find from the calculation only a very small RXE intensity for the transition to the $^1\Sigma^+$ state, which is configurationally mixed with σ-σ-type excitations and also interacts with Rydberg levels. We also find other close-lying $^1\Sigma^+$ states with admixture of the $1\pi^{-1}\pi^*$ configuration. RXE transitions to such correlation satellites might explain some of the weak bands observed in the RXE spectra of CO.

As seen in Table II, relative experimental intensities agree well with normalized values of the calculated transition intensities. The deviations in the resonant case might partially be due to that the experimental intensities for the broad $^1\Delta$ and $^1\Sigma^-$ bands are underestimated. The reason is that the simulated vibrational band profiles that were used to deduce the relative intensities from the experimental spectra are not reproducing the low-energy side of these broad bands very well.

D. Angular dependence

It is well known that x-ray emission from condensed samples with well-ordered crystal structures may be strongly anisotropic. It may be expected that x-ray emission from randomly oriented samples, such as gas-phase molecules, is isotropic. However, measurements with a polarization-selective x-ray-emission spectrometer have shown that the polarization [8] and angular [48] distributions from resonantly excited molecules are indeed anisotropic. In this work we show that a spectrometer that is not polarization selective

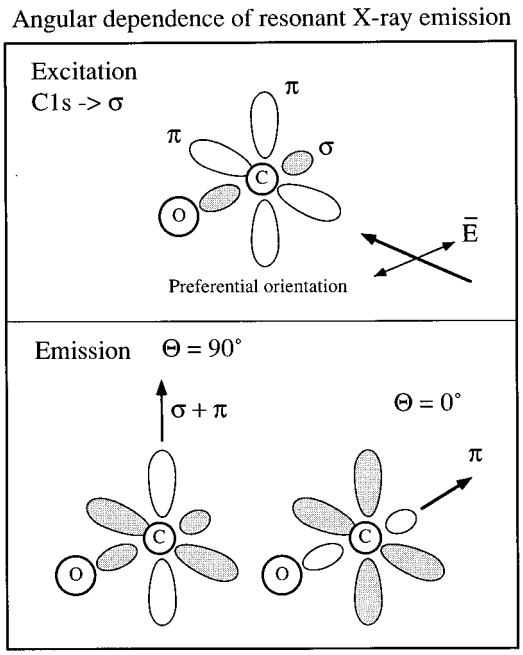

FIG. 5. Schematic picture illustrating the origin of the angular anisotropy in resonant x-ray emission (in the case of excitation to a σ orbital). The linear polarization of the synchrotron radiation and the symmetry of the core-excited state cause a preferential alignment of core-excited molecules. This preferential alignment leads to an anisotropic emission.

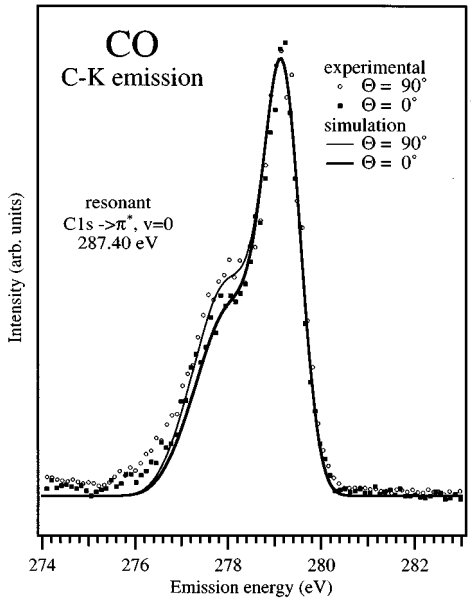

FIG. 6. Carbon π^* RXE spectra recorded at $\theta=0°$ and 90°. The spectra are normalized to the same peak height. Simulated emission profiles are included, for which the angular dependence (causing different relative intensities for the 5σ and 1π bands at the two angles) is accounted for.

can be used to measure the anisotropic angular dependence in RXE spectra. The experimental spectra were recorded at two angles, parallel ($\theta=0°$) and perpendicular ($\theta=90°$) to the polarization vector of the incident x-ray beam.

The angular dependence of RXE is caused by that the resonant excitations create an anisotropic ensemble of core-excited molecules. The direction of the preferential alignment, with respect to the linear polarization of the incident radiation, depends on the symmetry of the core-excited state (or to be precise, on the direction of transition dipole moment). The nuclear axis can be considered frozen during the x-ray-scattering process because of the relatively long period of time for any rotational motion. The alignment of the anisotropic ensemble of core-excited molecules determines the polarization and angular distribution of the resonant x-ray emission [49].

The angular dependence can be illustrated in a simple qualitative picture. For example, resonant excitations from a core to a σ orbital in CO tend to preferentially create excited molecules that are oriented with the internuclear axis parallel with the polarization vector of the incident x-ray beam, as illustrated in Fig. 5. The angular distribution of the x-ray emission depends on whether the core hole is filled by an electron from a π or σ orbital. For transitions where the core hole is filled by a σ electron the emission intensity has a minimum at $\theta=0°$ and a maximum at $\theta=90°$, whereas for transitions involving a π electron the minimum will be at $\theta=90°$ and the maximum at $\theta=0°$. A resonant core excitation to a π orbital, on the other hand, leads to that the core-excited molecules are preferentially aligned with their nuclear axis perpendicular to the linear polarization vector of the incident x-ray beam. The pattern of the angular distributions for π and σ emission shows an opposite trend in this case.

In Fig. 3 carbon Rydberg-excited RXE spectra recorded at $\theta=0°$ and 90° are presented. Significant variations of the intensity of the 1π band with respect to the intensity of the 5σ band can be observed. When the excitation is tuned to the C $1s$-$3s\sigma$ Rydberg resonance the relative intensity of the 1π band at $\theta=0°$ is much larger than it is at $\theta=90°$, whereas in the $3p\pi$ RXE spectra the relative intensity of the 1π band is larger at $\theta=90°$. These observations are in good agreement with what is predicted by the qualitative picture. However, for the π^* RXE spectra the angular dependence is very weak, as shown in Fig. 6. The reason that these spectra do not show stronger angular dependence cannot be given by the qualitative picture and the effect of orientational averaging must be taken into account.

It is possible to derive explicit formulas for the angular dependence of the x-ray emission from scattering theory applied to randomly oriented samples [14]. The intensities are expressed as

$$I(\theta)=I_{\perp}(\theta)+I_{\parallel}(\theta),$$

$$I_{\perp}(\theta)=\frac{1}{2}I_0[1-R],$$

$$I_{\parallel}(\theta)=\frac{1}{2}I_0[1+R(3\sin^2\theta-1)], \tag{5}$$

where θ is the angle between the polarization vector of the incident photon and the propagation direction of the outgoing photon. I_0 is proportional to the total intensity emitted in all directions and summed over all polarization vectors and

R is the polarization anisotropy parameter for each final state. The notations $\perp$ and $\parallel$ refer to the polarization direction of the emitted photon relative to a plane that is perpendicular to the Poynting vector of the incoming radiation. With a spectrometer that is not polarization selective it is not possible to measure directly $I_\perp$ or $I_\parallel$, but it is possible to measure the total intensity $I(\theta)$ as a function of emission angle θ. In our experiments we measured RXE spectra at $\theta=0°$ and 90°. We define

$$r=\frac{I(90°)}{I(0°)}=\frac{2+R}{2-2R}. \tag{6}$$

The general expressions for the anisotropy parameter R and the intensity I_0 have been evaluated in a previous paper [14]. It turns out that for a molecule like CO, in which only one core-excited electronic state at a time is involved in the process, the full scattering model including electronic interference effects and a two-step model, where the excitation and emission steps are separated from each other, give the same result.

Using group theory combined with the general formula for RXE transition elements in orientationally averaged molecules [13], we derive the following R values for different final states of a $C_{\infty v}$ molecule with Σ^+ ground-state symmetry:

$$R_{\Sigma^+}=\frac{2}{5},\quad R_\Pi=-\frac{1}{5},$$

$$R_\Delta=\frac{1}{10},\quad R_{\Sigma^-}=-\frac{1}{2}. \tag{7}$$

In the case of resonant excitation to a σ orbital the 5σ and 1π bands correspond to $^1\Sigma^+$ and $^1\Pi$ final states, respectively. The r values for the 5σ and 1π bands are given by

$$r_{5\sigma}^{\sigma}=2,\quad r_{1\pi}^{\sigma}=\frac{3}{4}. \tag{8}$$

When the core excitation involves an orbital of π symmetry, such as $3p\pi$, the final state of the 5σ band has $^1\Pi$ symmetry. The r value for the 5σ band is then given by

$$r_{5\sigma}^{3p\pi}=\frac{I_{5\sigma}(90°)}{I_{5\sigma}(0°)}=\frac{2+R_\Pi}{2-2R_\Pi}=\frac{3}{4}. \tag{9}$$

There are three possible final states when the core hole is filled by an electron from the 1π orbital: $^1\Sigma^+$,$^1\Delta$, and $^1\Sigma^-$. We have assumed that these final states are degenerate when the excitation is tuned to the $3p\pi$ resonance. The intensity of the 1π band at the two measured angles is then given by

$$I_{1\pi}(90°)=I_{\Sigma^+}(90°)+I_\Delta(90°)+I_{\Sigma^-}(90°),$$

$$I_{1\pi}(0°)=I_{\Sigma^+}(0°)+I_\Delta(0°)+I_{\Sigma^-}(0°). \tag{10}$$

If we also assume that the intensities can be related according to the statistical ratios $I_{\Sigma^+}=I_{\Sigma^-}=\frac{1}{2}I_\Delta$, we obtain

$$r_{1\pi}^{3p\pi}=\frac{I_{1\pi}(90°)}{I_{1\pi}(0°)}=\frac{(2+R_{\Sigma^+})+(2+R_{\Sigma^-})+2(2+R_\Delta)}{(2-2R_{\Sigma^+})+(2-2R_{\Sigma^-})+2(2-2R_\Delta)}=\frac{27}{26}. \tag{11}$$

Using these r values and assuming that the relative total integrated intensities I_0 for the 5σ and 1π bands are proportional to the relative intensities in the nonresonant case (Table II), the relative intensities at the two measured angles can be simulated. The relative intensities obtained were used to scale the simulated vibrational band profiles in Fig. 3. The agreement between the experimental and simulated spectra is very good, validating the model describing the angular dependence.

In the π^* RXE case we have a situation where one final state, the $^1\Sigma^+$ state, is not contributing to the *main* 1π band. The fact that the 5σ and 1π bands overlap in energy also makes the situation more complex. For the 5σ band we obtain the same relation for the r value as for excitation to a Rydberg orbital of π symmetry:

$$r_{5\sigma}^{\pi^*}=\frac{I_{5\sigma}(90°)}{I_{5\sigma}(0°)}=\frac{2+R_\Pi}{2-2R_\Pi}=\frac{3}{4}, \tag{12}$$

whereas for the 1π band, with the $^1\Sigma^+$ state not contributing, the r value is given by

$$r_{1\pi}^{\pi^*}=\frac{I_{1\pi}(90°)}{I_{1\pi}(0°)}=\frac{(2+R_{\Sigma^-})+2(2+R_\Delta)}{(2-2R_{\Sigma^-})+2(2-2R_\Delta)}=\frac{19}{22}. \tag{13}$$

The relation (13) is obtained under assumption that the $^1\Delta$ and $^1\Sigma^-$ states are degenerate and have statistical intensity ratios. Normalizing the r values for the 1π band to the r values for the 5σ band we obtain $r_{\text{norm}}^{3p\pi}=r_{1\pi}^{3p\pi}/r_{5\sigma}^{3p\pi}=\frac{18}{13}\approx 1.38$ in the Rydberg case and $r_{\text{norm}}^{\pi^*}=r_{1\pi}^{\pi^*}/r_{5\sigma}^{\pi^*}=\frac{38}{33}\approx 1.15$ in the π^* case. The latter value is closer to one, which explains that the π^* RXE spectra recorded at $\theta=0°$ and 90° appear to be almost identical in Fig. 6. Simulated spectra accounting for the small difference in angular dependence for the 5σ and 1π bands are compared with the experimental spectra in this figure. The simulated spectra reproduce the experimental ones very well, and that the relative intensities of the 5σ and 1π bands do not change more, at the two measured angles, can thus be attributed to the fact that the $^1\Sigma^+$ final state does not contribute to the observed 1π band.

If the spectrometer is polarization selective it will cause a change in the observed relative intensities (the r values). For the spectrometer used in these experiments a 10–20 % difference in efficiency for $I_\perp$ and $I_\parallel$ has been measured [50]. This small polarization selectivity does not, however, change the r values significantly [51].

V. SUMMARY

It is instructive to use the present results for the CO molecule to stress some characteristic differences and similarities between resonant and nonresonant x-ray-emission spectra. In both cases the spectral quality and resolution have reached a point where not only different electronic transitions are separated but also where vibronic factors are relevant. Although vibronic fine structures remain unresolved in this work, the analysis of the band profiles called for detailed information of potential-energy curves and interference effects between close-lying vibrational levels.

As shown here, nonresonant and resonant x-ray spectra of CO are quite similar when the resonant core excitation involves a Rydberg orbital. The interaction of a spectator electron in a Rydberg orbital with the remaining electron cloud is thus not sufficiently large to change either energies or intensities in the x-ray-emission spectra to any appreciable extent. We find that the relative intensities and vibrational band shapes can be simulated with good agreement using the same potential-energy curve parameters and relative intensities as used to simulate the nonresonant carbon spectrum. The energy shifts in the Rydberg-excited spectra are found to be 0.5 eV or less.

In the π^* RXE spectra, on the other hand, the spectator transitions have large energy shifts in comparison to the corresponding transitions in the nonresonant spectra, which can be attributed to the screening nature of the *penetrating* π^* electron. The screening effects are different when the core hole is situated on the carbon or oxygen site and whether a 5σ or a 1π electron fills the core hole, because of the localization with respect to the core-hole site of the orbitals involved in the RXE process. Energy shifts calculated by multiconfigurational self-consistent field theory were found to compare well with experimental data. Center-of-gravity corrections of the vertical approximation are significant for such comparisons. In all of the cases investigated the effect of relaxation is found to be important for both screening energies and intensities. We found that the presence of the π^* electron significantly enhances the relative intensity for the 5σ band in the oxygen spectrum, while other transitions studied conform with the notion that screening intensities tend to be small [29]. Special effects, as exemplified here by the displacement and intensity depletion of the $1\pi^{-1}\pi^{*\,1}\Sigma^{+}$ multiplet may still cause apparent intensity screening.

Regarding the angular distributions, we find here, in analogy with polarization dependence [8,14,49] and parity selection [6,12], that the discrete nature of the core-excited states prepares favored directions for the x-ray emission and that the dipole character of the absorption and emission then leads to a specific angular distribution pattern (specific polarization anisotropy, specific parity selection) with no counterpart in nonresonant emission spectra. In the nonresonant case the core electron is excited to the continuum, which is infinitely degenerate, representing all symmetries. This makes the nonresonant process much less selective with respect to any of the processes mentioned here.

ACKNOWLEDGMENTS

This work was supported by Göran Gustafssons Foundation for Research in Natural Sciences and Medicine and by the Swedish Natural Science Research Council (NFR). The experiments were performed at the ALS, of Lawrence Berkeley Laboratory, operated by the DOE under Contract No. DE-AC03-76SF00098.

[1] J. Nordgren, in *Proceedings of the 11th International Conference on Vacuum Ultraviolet Radiation Physics, 1995, Tokyo*, edited by T. Miyahara, Y. Azuma, M. Watanabe, and T. Ishii (Elsevier Science, Amsterdam, 1996); J. Electron. Spectrosc. Relat. Phenom. **78**, 25 (1996).

[2] F.Kh. Gel'mukhanov, L.N. Mazalov, A.V. Nikolaev, and A.V. Kondratenko, Chem. Phys. Lett. **46**, 133 (1977).

[3] F. Kaspar, W. Domke, and L.S. Cederbaum, Chem. Phys. **44**, 33 (1979).

[4] N. Correia, A. Flores-Riveros, H. Ågren, L.K. Helenelund, L. Asplund, and U. Gelius, J. Chem. Phys. **83**, 2035 (1985).

[5] N. Wassdahl, A. Nilsson, T. Wiell, H. Tillborg, L.-C. Duda, J.-H. Guo, N. Mårtensson, J. Nordgren, J.N. Andersen, and R. Nyholm, Phys. Rev. Lett. **69**, 812 (1992).

[6] P. Glans, K. Gunnelin, P. Skytt, J.-H. Guo, N. Wassdahl, J. Nordgren, H. Ågren, F.Kh. Gel'mukhanov, T. Warwick, and E. Rotenberg, Phys. Rev. Lett. **76**, 2448 (1996).

[7] R. Mayer, D.W. Lindle, S.H. Southworth, and P.L. Cowan, Phys. Rev. A **43**, 235 (1991).

[8] D.W. Lindle, P.L. Cowan, R.E. LaVilla, T. Jach, and R.D. Deslattes, Phys. Rev. Lett. **60**, 1010 (1988).

[9] E.D. Poliakoff, J.L. Dehmer, D. Dill, A.C. Parr, K.H. Jackson, and R.N. Zare, Phys. Rev. Lett. **46**, 907 (1981).

[10] F.P. Larkins and A.J. Seen, Phys. Scr. **41**, 827 (1990); F.P. Larkins, Nucl. Instrum. Methods Phys. Res. Sect. B **87**, 215 (1994).

[11] A. Flores-Riveros and H. Ågren, Phys. Scr. **44**, 442 (1991).

[12] F.Kh. Gel'mukhanov and H. Ågren, Phys. Rev. A **49**, 4378 (1994).

[13] Y. Luo, H. Ågren, and F.Kh. Gel'mukhanov, J. Phys. B **27**, 4169 (1994).

[14] Y. Luo, H. Ågren, and F.Kh. Gel'mukhanov, Phys. Rev. A **53**, 1340 (1996).

[15] Y. Luo, H. Ågren, J.-H. Guo, P. Skytt, N. Wassdahl, and J. Nordgren, Phys. Rev. A **52**, 3730 (1995).

[16] Y. Luo, H. Ågren, J.-H. Guo, P. Skytt, N. Wassdahl, and J. Nordgren, Phys. Rev. B **52**, 14 479 (1995).

[17] P. Skytt, J.-H. Guo, N. Wassdahl, J. Nordgren, Y. Luo, and H. Ågren, Phys. Rev. A **52**, 3572 (1995).

[18] P. Skytt, C.-J. Englund, J.-H. Guo, P. Glans, K. Gunnelin, N. Wassdahl, and J. Nordgren (unpublished).

[19] T. Warwick, P. Heimann, D. Mossessain, W. MacKinney, and H. Padmore, Rev. Sci. Instrum. **66**, 2037 (1995).

[20] J. Nordgren, G. Bray, S. Cramm, R. Nyholm, J.-E. Rubensson, and N. Wassdahl, Rev. Sci. Instrum. **60**, 1690 (1989).

[21] Custom-made window from Metorex International Oy, P.O. Box 85, FIN-02201 Espoo, Finland.

[22] J.-H. Guo, N. Wassdahl, P. Skytt, L.-C. Duda, S. Butorin, C.-J. Englund, and J. Nordgren, Rev. Sci. Instrum. **66**, 1561 (1995).
[23] H. Ågren, A. Flores-Riveros, and H.J.Aa. Jensen, Phys. Scr. **40**, 745 (1989).
[24] H.J.Aa. Jensen, H. Ågren, and J. Olsen, in *Modern Techniques in Computational Chemistry*, edited by Enrico Clementi (ESCOM Science, Leiden, 1990), p. 435.
[25] P.Å . Malmquist, Int. J. Quantum Chem. **30**, 479 (1986).
[26] H.J.Aa. Jensen, P. Jørgensen, and H. Ågren, J. Chem. Phys. **87**, 451 (1987).
[27] P.-O. Widmark, P.Å. Malmquist, and B.O. Roos, Theor. Chim. Acta **77**, 291 (1990).
[28] A. Naves de Brito, N. Correia, S. Svensson, and H. Ågren, J. Chem. Phys. **95**, 2965 (1991).
[29] H. Ågren, Y. Luo, F.Kh. Gel'mukhanov, and H.J.Aa. Jensen, J. Electron Spectrosc. (to be published).
[30] R. Manne, J. Chem. Phys. **52**, 5733 (1970).
[31] H. Ågren and R. Arneberg, Phys. Scr. **28**, 80 (1983).
[32] J. Nordgren and H. Ågren, Comments At. Mol. Phys. **14**, 203 (1984).
[33] N. Wassdahl, G. Bray, S. Cramm, P. Glans, P. Johansson, R. Nyholm, N. Mårtensson, and J. Nordgren, Phys. Rev. Lett. **64**, 2807 (1990); R.C.C. Perera, P.L. Cowan, D.W. Lindle, R.E. LaVilla, T. Jach, and R.D. Deslattes, Phys. Rev. A **43**, 3609 (1991).
[34] A. Flores-Riveros, N. Correia, H. Ågren, L. Pettersson, M. Bäckström, and J. Nordgren, J. Chem. Phys. **83**, 2053 (1985).
[35] H. Ågren, L. Selander, J. Nordgren, C. Nordling, and K. Siegbahn, Chem. Phys. **37**, 161 (1979).
[36] U. Gelius, S. Svensson, H. Siegbahn, E. Basilier, Å. Faxälv, and K. Siegbahn, Chem. Phys. Lett. **28**, 1 (1974).
[37] O. Goscinski and A. Palma, Chem. Phys. Lett. **47**, 322 (1977).
[38] H. Ågren, Chem. Phys. Lett. **83**, 149 (1981).
[39] P. Skytt, P. Glans, K. Gunnelin, J.-H. Guo, and J. Nordgren, following paper, Phys. Rev. A **55**, 146 (1997).
[40] K.P. Huber and G. Herzberg, *Molecular Spectra and Molecular Structure IV* (Van Nostrand Reinhold, New York, 1979).
[41] M. Tronc, G.C. King, and F. Read, J. Phys. B **12**, 137 (1979).
[42] S.J. Osborne, A. Ausmees, S. Svensson, A. Kivimäki, O.-P. Sairanen, A. Naves de Brito, H. Aksela, and S. Aksela, J. Chem. Phys. **102**, 7317 (1995).
[43] A.P. Hitchcock and C.E. Brion, J. Electron. Spectrosc. Relat. Phenom. **18**, 1 (1980).
[44] M. Neeb, J.-E. Rubensson, M. Biermann, W. Eberhardt, K.J. Randall, J. Feldhaus, A.L.D. Kilcoyne, A.M. Bradshaw, Z. Xu, P.D. Johnsson, and Y. Ma, Chem. Phys. Lett. **212**, 205 (1993).
[45] M. Domke, C. Xue, A. Puschmann, T. Mandel, E. Hudson, D.A. Shirley, and G. Kaindl, Chem. Phys. Lett. **173**, 122 (1990).
[46] B. Wannberg, D. Nordfors, K.L. Tan, L. Karlsson, and L. Mattson, J. Electron. Spectrosc. Relat. Phenom. **47**, 147 (1988).
[47] B.F. Minaev, N.M. Ivanova, and Z.M. Muldahmetov, Spectrosc. Lett. **22**, 901 (1989).
[48] S.H. Southworth, D.W. Lindle, R. Meyer, and P.L. Cowan, Phys. Rev. Lett. **67**, 1098 (1991).
[49] F.Kh. Gel'mukhanov and L.N. Mazalov, Opt. Spektrosk. **42**, 659 (1977) [Opt. Spectrosc. (USSR) **42**, 371 (1977)].
[50] A value estimated from the measured angular distribution of the π and σ bands in x-ray-emission spectra from highly oriented pyrolytic graphite (unpublished results).
[51] Assuming that the efficiency for detection of $I_{\parallel}$ is 20% lower than of $I_{\perp}$ results in that $r=(3+R)/(3-3R)$. Using this formula, we obtain, for example, the normalized r values $r^{3p\pi}_{\rm norm}=\frac{121}{91}\approx 1.33$ and $r^{\pi^*}_{\rm norm}=\frac{87}{77}\approx 1.13$. These values are just slightly lower than those calculated under the assumption that the spectrometer has no polarization selectivity.